INL/JOU-23-71080-Revision-0

Analysis of the Laser Welding Keyhole using Inline Coherent Imaging

October 2022

Changing the World's Energy Future

Tate Patterson, Boyd Panton, John C. Lippold

Idaho National Laboratory

INL/JOU-23-71080-Revision-0

Analysis of the Laser Welding Keyhole using Inline Coherent Imaging

Tate Patterson, Boyd Panton, John C. Lippold

October 2022

Idaho National Laboratory
Idaho Falls, Idaho 83415

http://www.inl.gov

Prepared for the
U.S. Department of Energy
Under DOE Idaho Operations Office
Contract 1822144

Analysis of the Laser Welding Keyhole using Inline Coherent Imaging

Authors: T. Patterson[1], B. Panton[2], J. Lippold[2]

1
Corresponding Author
Contact: tate.patterson@inl.gov
Energy and Environment Science and Technology
Idaho National Laboratory
Idaho Falls, ID, USA

2
Welding Engineering Program
Department of Materials Science and Engineering
The Ohio State University
Columbus, OH USA

Abstract

Laser beam welding is a widely used fusion welding process in many industrial applications such as automotive, aerospace, energy, defense, and medical products. Industry has a fundamental need to model the laser welding process to minimize experimental testing and improve confidence in production welds. However, computational models attempting to predict weld formation are limited by an incomplete understanding of the beam-material interactions. As a consequence, these models do not accurately predict the mechanisms associated with laser weld formation. To improve the current state of prediction capabilities, it is vital to better detect/measure the physical aspects of the weld pool during high energy density welding. In this work, a novel real-time laser weld monitoring device using inline coherent imaging (ICI) was used to provide a fundamental understanding of laser weld formation via vaporization.

The objective of this work was to investigate and quantify the relationship relating laser weld parameters and the vapor capillary (keyhole) through a state-of-the-art measurement technique. Bead-on-plate laser beam welds were produced with partial penetration on 304L stainless steel, 2205 duplex stainless steel, and Ti-6Al-4V. Keyhole monitoring was performed using a commercially available ICI system to collect keyhole penetration data in real time. These measurements were reconstructed to generate the vapor capillary shape at different welding parameters. Process parameters significantly influenced the keyhole shape and the keyhole root position relative to the process beam. The keyhole geometry showed distinct differences between the stainless steel alloys and Ti-6Al-4V.

Keywords: laser beam welding, inline coherent imaging, weld penetration, 304L, 2205, Ti-6Al-4V

Introduction

Laser beam welding (LBW) is commonly performed autogenously (i.e., without filler material) and within two distinct modes of penetration, dependent on the application. The laser beam (LB) welds are usually categorized as conduction or "keyhole" mode. The distinction between these two modes are loosely based on depth-to-width aspect ratios less than one (conduction) or greater than one (keyhole) [1,2].

Welds produced in conduction mode are a result of low power density and/or short interaction times (i.e., high travel speed). These welds produce a transverse shape similar to arc welding processes. The heat input to the material surface results in thermal diffusion or conductive heat transfer into the underlying material. The combination of conductive heat loss and fluid flow (weld pool convection) results in the characteristic weld size and shape [3]. Conduction mode welding is advantageous relative to keyhole mode welding due to a higher probability of producing welds free of defects by avoiding instabilities associated with vaporization. Conduction mode also has a reduced chance of missing the joint because of wider weld pools. However, penetration is limited in conduction mode welding, and a failure to induce a weld pool depression results in low laser coupling and melting efficiencies.

Deep penetration welding, known as keyhole mode, requires simultaneous melting and vaporization. The benefits to keyhole mode are deep penetration, low heat input, higher coupling efficiencies, and narrow heat affected zones [1,4]. The formation of a vapor capillary is a result of vaporization developing a recoil force to depress the liquid weld pool [5,6]. The power density is high enough that conduction, convection, and radiation heat loss is inadequate at removing heat from the incident beam. The complexity of the solid–fluid–vapor–beam interaction phenomena governing keyhole formation induces transient events [7,8] between the beam and the weld pool. Instability of the keyhole can be a major issue and lead to root spiking defects, keyhole collapse, and spatter generation [9]. The collapse of the vapor cavity then induces pore formation through entrainment of atmospheric air and/or shielding gas that cannot float out prior to solidification. The transient nature of the keyhole also increases the difficulty in fully understanding the mechanisms involved during keyhole mode welding.

However, ambiguity exists when the weld parameters are such that neither full conduction nor full keyhole mode is exhibited in the resultant weld cross-section. The power density and interaction time is such that conduction mode is present with the onset of vaporization and weld pool depression. Aspect ratios and power densities are used to differentiate between keyhole and conduction [10], but the values are only approximations. The actual welding condition is dependent on wavelength, beam diameter, power, travel speed, and the material under investigation [11].

As with the heat source characteristics, the material properties contribute to the variation in weld pool formation and the distinction between conduction mode and keyhole mode. There is considerable information in the open literature describing beam interactions and weld pool development [12–19]. However, the actual physics of the high energy density (HED) welding processes are extremely complex. This is particularly evident with advancement of optic systems that can raster or oscillate the beam in user-defined patterns. During oscillatory or “wobble” welding, the beam velocity is no longer a fixed value and varies at each point along the scan pattern. This oscillation complexity has yet to be sufficiently modeled in the current literature.

The conventional techniques for understanding the keyhole is through high speed videography [20] of the weld surface or through in-situ x-ray imaging [14,21,22]. High speed videos are limited to observing the keyhole location within the melt pool on the surface, generating information with limited use to further understand the process dynamics. X-ray imaging is restricted to one-dimension but can capture the keyhole shape from a longitudinal cross section view. Historically, these x-ray images are low in resolution resulting in crude extrapolations of the profiles [14,23]. However, Cunningham et al. [21] recently utilized synchrotron x-ray imaging to capture the keyhole dynamics with high temporal and spatial temporal resolutions (2 µm and 50-400 kHz). They showed keyhole transitions going from a low depth-to-width aspect ratio vapor depression to a region with an aspect ratio of nearly 1:2 with high keyhole instability. It was reported that these transitions and the traditional “conduction mode” classification based on a metallographic section does not represent vaporization and a weld pool depression. It should be noted that these “welds” were actually laser powder bed additive manufacturing deposits, so that the correlation to actual welding may be limited [21].

Optical coherence tomography (OCT) is a measurement technique that utilizes low-coherence interferometry and a broad-band light source. This technique is based on Michelson interferometry [24]. The inline coherent imaging (ICI) terminology stems from using the OCT technique and projecting the beam coaxially or “inline” with the laser process beam [24–26]. Bandwidth determines the resolution, and Fraser [27] reported resolutions as low as 5-10 µm with acquisition rates reported as high as 300 kHz using CMOS cameras [25]. More details of the ICI system and its operation can be found elsewhere [24,28,29].

The term tomography in OCT suggests that the technique can represent a cross-section through a solid object such as in ultrasonic or x-ray imaging. This is possible in biological tissues where OCT was previously implemented but is not the case in metallic applications where the photons are not transparent with the solid. Therefore, it should not be confused with internal imaging. Perhaps this is why Dorsch et al. [30] mislabeled it as optical computed “topography”. However, ICI imaging has practical potential for real-time monitoring of workpiece height, joint gap, and weld penetration during deep penetration LBW when a vapor depression (or cavity) exists in the weld pool [25,31–33].

Because the ICI system works by reflecting light back from the keyhole wall and measuring optical path length, only conditions producing ideal, straight-line reflections generate a correct depth measurement. Figure 1 shows a schematic with ray tracing demonstrating how different keyhole geometries influence the light reflection back to the detector [23]. The first condition (Fig. 1a) produces a correct measurement based on a direct "line of sight". However, an incident photon reflecting off the keyhole wall multiple times before returning to the detector would result in a length measurement that is a sum of those reflections. This is shown in Fig. 1b. Similarly, features on the keyhole wall caused by abnormal geometries or fluctuations during the process will reflect the photons back to the detector and provide false indications of keyhole depth, as in Fig. 1c. It is also likely that a photon will never return to the detector and become absorbed within the keyhole or exit the keyhole at an angle inconducive to detection, as shown in Fig. 1d.

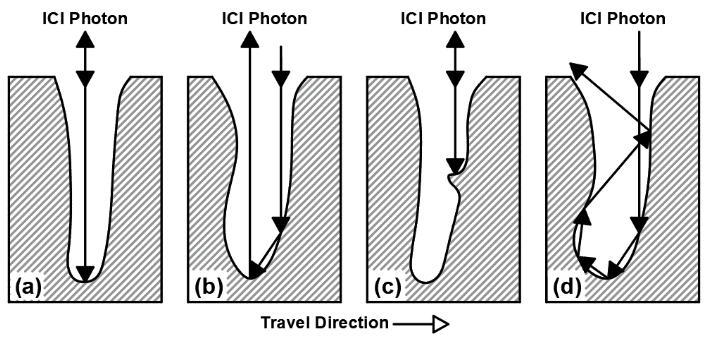

Figure 1. Influence of keyhole geometry on ICI measurements. Recreated and modified from Boley et al. [23].

Webster et al. [34] reported that ICI can detecting pore formation. Although, in their study pore detection was only shown by varying the power and transitioning between two drastically different penetration depths. Boley et al. [23,35] reported that the region that contained greater noise may coincide with locations of porosity. However, ICI is not necessarily sensitive enough to distinguishing pore locations. The issue is mostly represented by the fundamental mechanism depicted in Fig. 1. Most likely, pore formation may only be indirectly monitored, or inferred, through the detection of keyhole instability.

The objective of this research was to utilize a commercial ICI system to map the keyhole geometry and provide a fundamental understanding relating the measurable keyhole features to LB process parameters. Partial penetration, bead-on-plate LB welds were produced while using the ICI system to compile depth measurements across the weld pool. All welds were metallurgically evaluated to analyze the penetration and transverse section width characteristics. Commercial alloys of 304L stainless steel (SS), 2205 duplex stainless steel (DSS), and Ti-6Al-4V were evaluated for an understanding of vaporization and the weld pool depressions relative to LB parameters in the different alloys.

Experimental Procedures

The following section defines the welding procedures, material preparation methods, measurement techniques, and material compositions. The laser welds were bead-on-plate only (no joint). The welding parameters were controlled such that the greatest penetration was maximized at ≈2/3 of the workpiece thickness (3/16 inches or 4.76 mm).

Laser Parameters and Weld Procedures

The laser was an IPG Photonics® YLS-6000 (Yb^{3+}-doped) fiber laser. The optics were an IPG Photonics® D50 Wobble Head with a 150 mm collimating lens and a 300 mm focusing lens, and the fiber diameter was 300 µm. The focal beam diameter was 600 µm and confirmed with a Primes Focus Monitor FM120 [29,36]. The analog-digital converted data measured via the focus monitor was extracted and processed using script developed in Matlab® software. This script computed the beam diameter based on the second moment (D2M) as defined in ISO 11146 [37]. A plot showing the three-dimensional representation of the measured intensity distributions for multiple beam locations at 1600 W of power are shown in Figure 2. Scans were recorded at 1.47 mm increments along the beam axis after determining the beam waist position. The Rayleigh length was determined to be ≈8 mm. The beam parameter product (BPP) was 10 mm*mrad with an M^2 value of ≈30. Welding was performed at the focal position and distribution shown in Fig. 2b.

The laser power was confirmed with an Ophir 10K-W-BB-45-V3 power sensor connected to an Ophir Juno power meter and StarLab software (v3.6.2). It should be noted that all the reported laser powers are based on the measured value and not the setting within the laser power supply. More detail on this is provided in Reference [29].

The welding setup used moveable optics attached to a Yaskawa Motoman MC2000 robot controlled with a DX100 controller. Argon shielding gas was applied trailing and leading the weld at 45 CFH (≈21 LPM) and ≈3 mm above the plate surface. A jet of compressed air was applied approximately 10 mm above the plate surface at the beam position to mitigate plume–beam interactions. Photographs and more information on the shielding setup is available in Reference [29]. Scale removal was performed on all alloys using a fly cutter on a milling machine and were welded in the as-machined condition. The materials were at room temperature (≈20°C) prior to each weld. Welds were performed with lengths necessary to acquire the resolution of the ICI system, and the resolution is discussed in the following section. Thus, faster travel speeds required longer weld lengths.

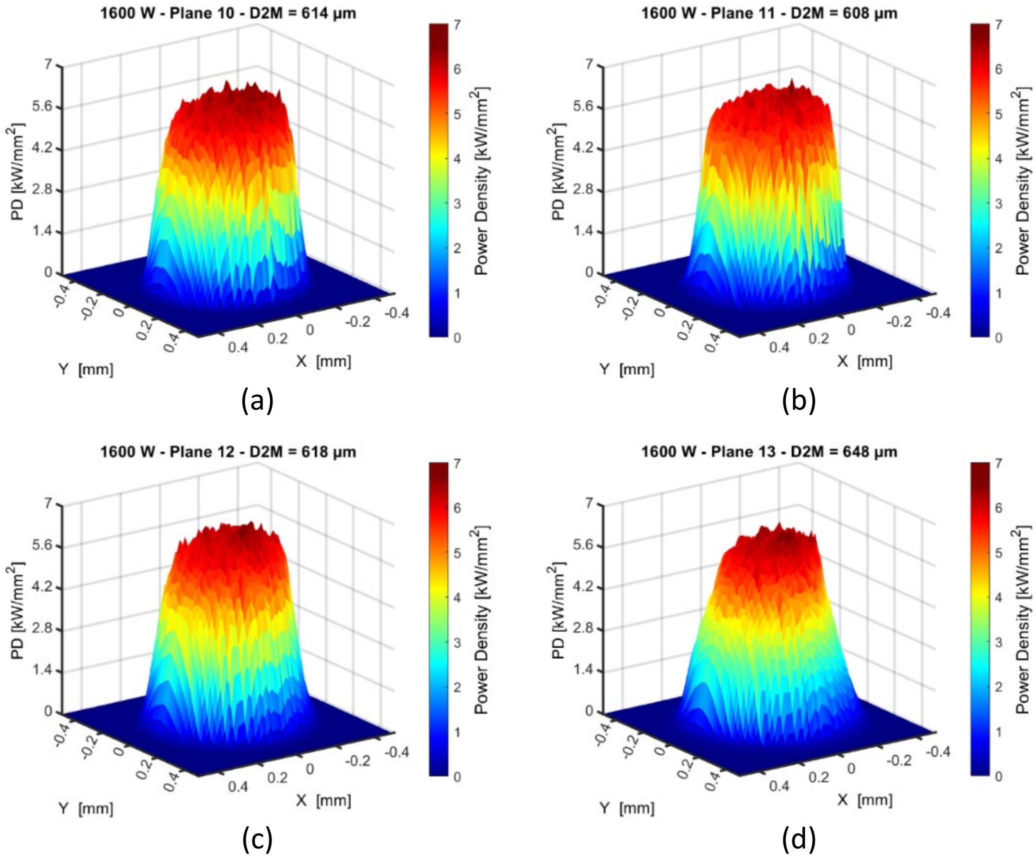

Figure 2. Laser intensity distributions at 1600 W of power through the beam waist or focal point used on all alloys investigated. a) 1.47 mm above beam waist, b) beam waist, c) 1.47 mm below beam waist, and d) 2.94 mm below the beam waist. The measured beam diameter was based on the second moment diameter [37] *and abbreviated as D2M.*

Inline Coherent Imaging

The ICI approach utilized a Laser Depth Dynamics^{TM} 700 (LDD-700^{TM}) system with a LD-700-OM1M-2 optics module and the 3DM3R beam coupler. This setup had a 6 mm field of view for depth detection. The superluminescent diode (SLD) broad-band wavelength was 800-900 nm [38]. The software was IPG OmniWeld^{TM} v2.5.2.5 [38]. The theoretical ICI beam diameter is ≈25 µm [24], but the actual ICI beam was not measured and is likely larger than the theoretical value. The ICI system used a 5 µm diameter feed fiber and a 30 mm collimating lens. With the 300 mm focal length lens in the process optics, the calculated ICI beam diameter is 50 µm. However, the LDD-700^{TM} system uses a proprietary configuration to further reduce the beam diameter by half.

All ICI calibrations were performed according to the manufacturer's procedures. For calibrating the (x,y) ICI beam position with the process beam, a short duration laser pulse at low power was made on the 304L SS plate. The process laser parameters were adjusted to achieve the smallest diameter spot or melt region possible, which was ≈1000 µm. Using the three-dimensional (3D) scan utility, the ICI scan origin was positioned by shifting crosshairs within the software to the greatest depth in the laser spot. This point was defined as the (0,0) process beam and ICI beam position. For validation, this procedure was repeated twice more. Further information about the ICI system setup is provided in Reference [29].The ICI system was only used in the manufacturer's keyhole tracking mode. This feature was designed for detecting the keyhole locations relative to the process beam. But to better understand keyhole formation from a fundamental perspective, the data was extracted from the system and further processed. Figure 3 represents a longitudinal view of the ICI beam. The ICI beam is smaller than the process beam and manipulated to scan larger areas as defined by the user. For the stainless steel alloys, the scan size was 1200x1200 µm in the x-y direction. For Ti-6Al-4V, the scan size was increased to 2000x2000 µm to capture the wider opening at the top of the keyhole. The data collection was maximized in the ICI system to 800x800 data points with a 200 kHz sampling frequency. This resolution resulted in 667 samples/mm for the stainless steels and 400 samples/mm for Ti-6Al-4V. It should be noted that this resolution is based on a scan using stationary process optics and not traveling as depicted in Figure 4.

The system tracks each x-y location and outputs a depth measurement assuming a reflection is returned to the detector. Similarly, Figure 4 shows a schematic to illustrate how the beam was deflected with a predefined width and acquired the data throughout the length of the weld. Therefore, the results in this study are based on a compilation of data points throughout the length of the weld and do not represent a single *in-situ* measurement. To avoid detection of transient events during weld initiation, the ICI measurement was delayed by 200 ms relative to the start of the weld.

Post processing of the extracted ICI data to analyze keyhole root depth, keyhole volume, and keyhole diameters was performed via code developed in MATLAB® software. The techniques used to perform these operations and the code is provided in detail in Reference [29].

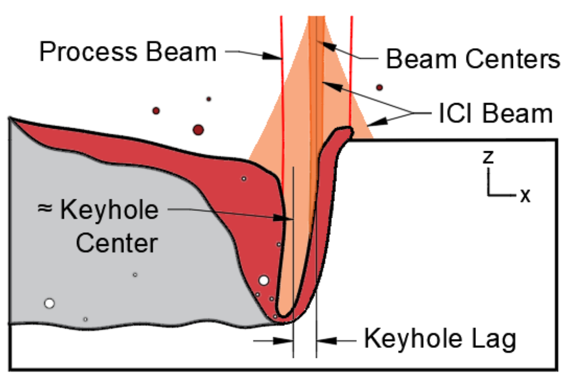

Figure 3. Schematic of ICI beam coaxial with the process beam and scanned across the keyhole.

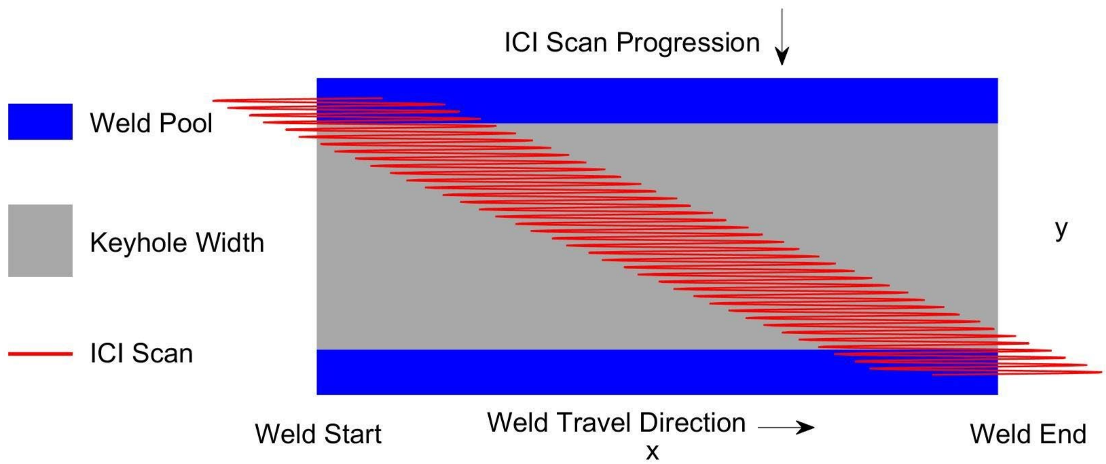

Figure 4. Schematic of the ICI scan progression from the start of the weld (left) to the end of the weld (right) with the scan progressing across the keyhole as the weld progresses.

Materials

The chemical compositions of Type 304L SS and 2205 DSS are shown Table 1, and the chemical composition of Ti-6Al-4V is shown in Table 2. The chemical compositions, excluding carbon, hydrogen, nitrogen, oxygen, and sulfur, were measured with optical emission spectroscopy (OES). The reported OES measured values are an average from three measurements.

For stainless steel, carbon (C) and sulfur (S) were measured using combustion analysis. Nitrogen (N) and oxygen (O) were measured with inert gas fusion. These composition measurements were completed according to ASTM E1019-18 [39]. For Ti-6Al-4V, carbon was measured via combustion analysis based on ASTM E1941 [40]. Oxygen and nitrogen were measured via inert gas fusion according to ASTM E1409 [41]. Hydrogen was measured via inert gas fusion thermal conductivity/infrared detection according to ASTM E1447 [42]. All other elements were reported based on the OES measurement.

Metallographic preparation involved cutting, mechanical grinding, and polishing as described in References [29] and [43]. Electro-chemical etching was performed for the SS alloys using 60% nitric acid and 40% distilled water with a constant voltage of 1.5V for ≈20 seconds. The Ti-6Al-4V samples were etched for ≈30 seconds using the developed reagent consisting of 10 mL HF, 40 mL HCl, and 50 mL H_2O [29,43]. The macrographs were captured with an Olympus® GX51 inverted microscope.

Table 1. Chemical compositions in weight percent for Type 304L SS and 2205 DSS with an iron (Fe) balance.

Alloy	Cr	Mo	Si	Nb	Ni	Mn	Cu	C*	N*	S*	P*
304L	18.2	0.30	0.28	0.020	8.14	1.23	0.50	0.030	0.065	0.001	0.027
2205	22.3	3.02	0.32	0.010	5.40	1.76	0.31	0.025	0.15	0.001	0.032

**Measured via LECO combustion or inert gas fusion according to ASTM E1019* [39].

Table 2. Chemical compositions in weight percent for Ti-6Al-4V.

Alloy	Ti	Al	O*	N*	C*	V	Nb	Fe	Si	H*
Ti-6Al-4V	89.4	6.27	0.18	0.0083	0.021	4.00	0.033	0.18	0.013	0.0051

**Measured via LECO combustion, inert gas fusion, or thermal conductivity/ infrared according to ASTM E1941* [40]*, E1409* [41]*, or ASTM E1447* [42].

Results and Discussion

The compilations of depth measurements throughout the weld lengths were analyzed in various orientations to use the ICI system to expand the current understanding of keyhole formation. The usefulness of the ICI data is to support the underlying mechanisms behind keyhole formation relative to the influences of weld pool convection [44]. It was postulated that this information can show the variation between the vapor depression and the weld pool depth. Specifically, the motivation for using the ICI system was to quantify the shape, position, and volume of the keyhole or vapor capillary as it relates to process parameters. It is also of interest to characterize the region where a vapor depression/vapor capillary initially forms and relate this to the metallographic section of that region. The weld cross-sections relating to each 304L, 2205, and Ti-6Al-4V ICI scan is shown in Figures 5 and 6 for 1000 W and 1600 W, respectively. Each weld section was extracted from a steady-state location near the center of the weld length.

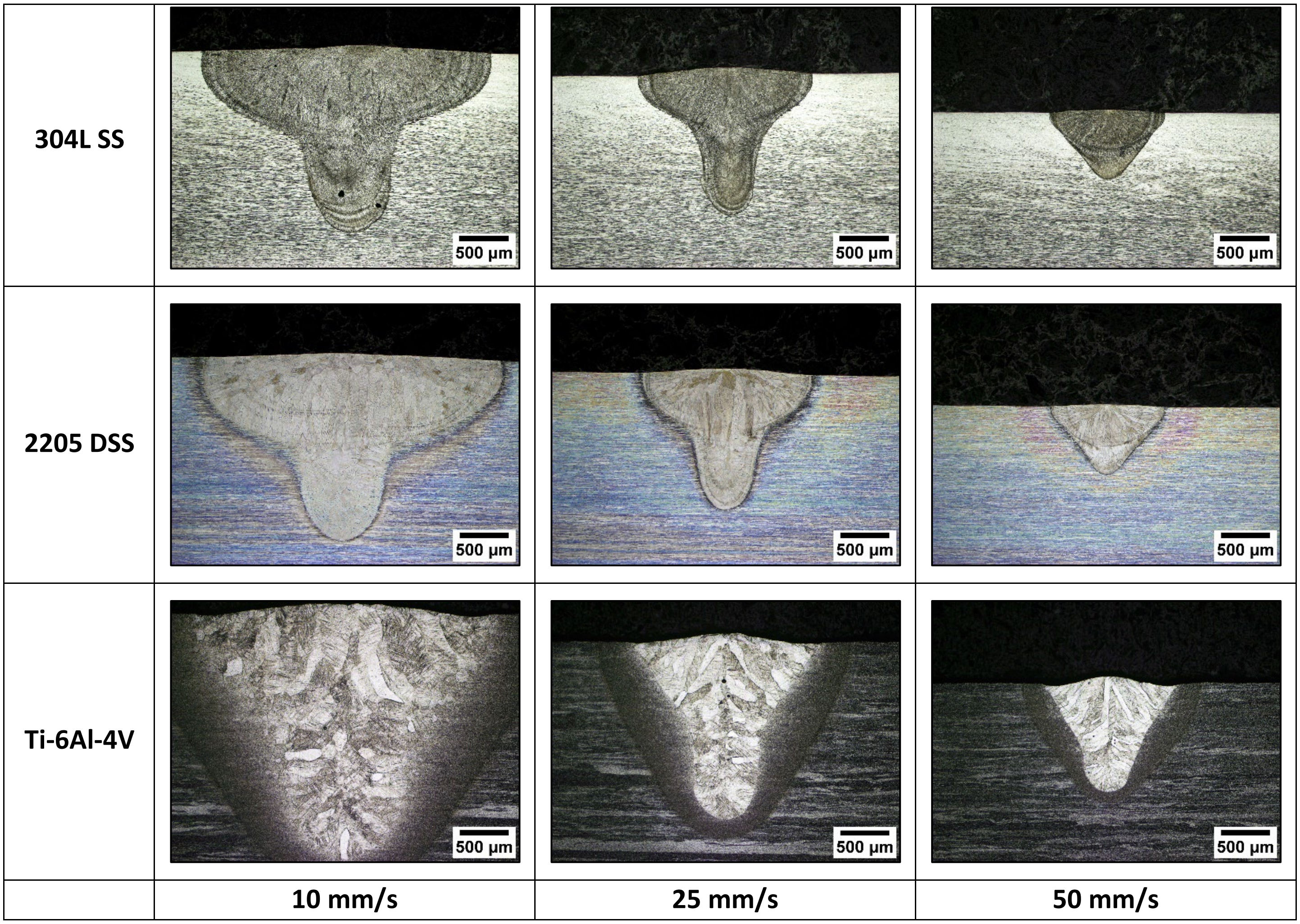

Figure 5. Laser beam weld transverse cross-sections at 1000 W.

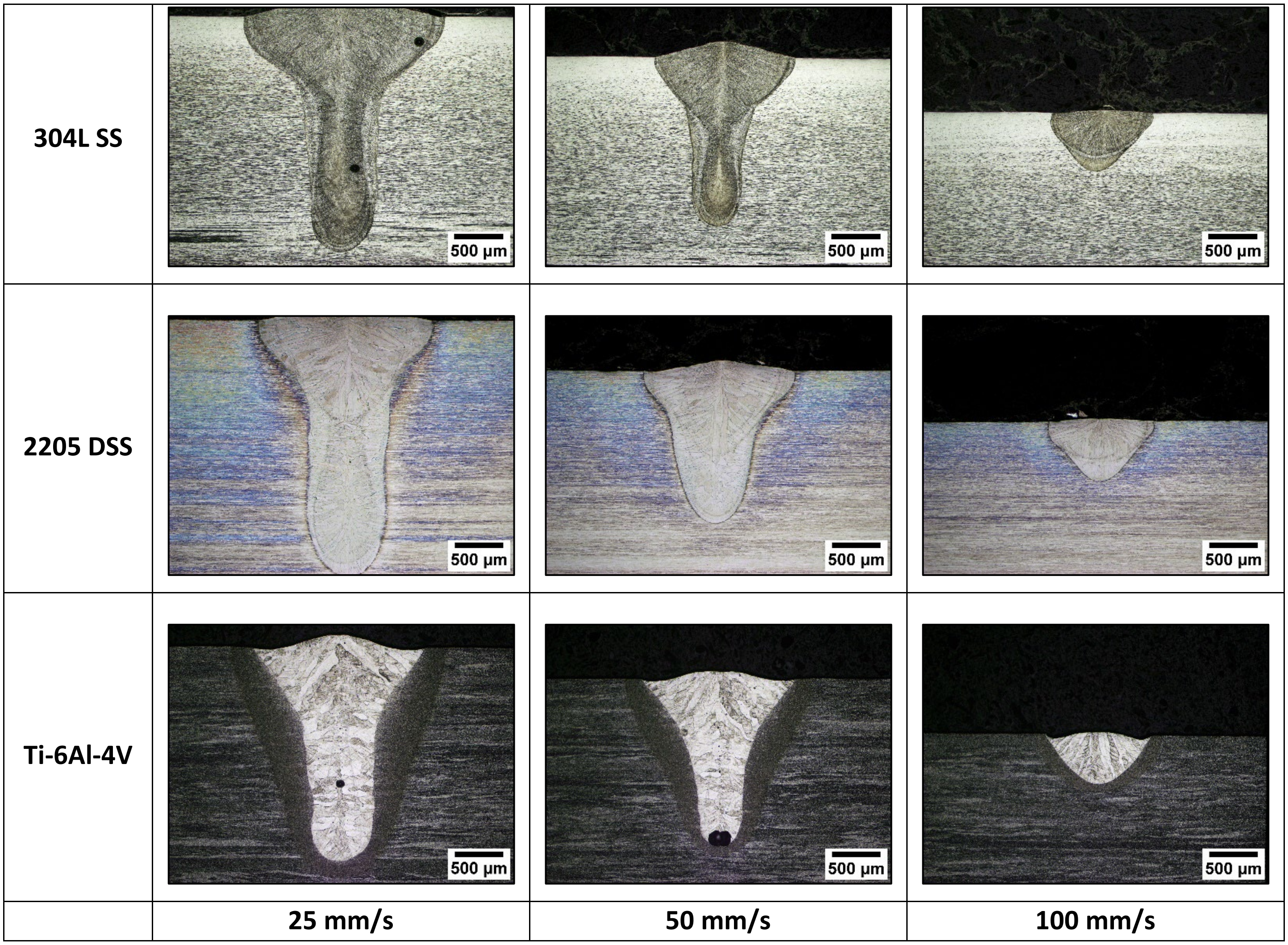

Figure 6. Laser beam weld transverse cross-sections at 1600 W.

By post processing a compilation of depth measurements collected along the weld length, the 3D data was evaluated through projections at different orientations. A surface view of keyhole scans for 304L SS at 1600 W and travel speeds of 25 mm/s and 50 mm/s are shown in Fig. 7a and Fig. 7b, respectively. The color scale represents the depth of the individual measurements. The individual data points are not representative of the ICI beam size and are only for visualization. In Fig. 7, the regions mapped via the ICI system do not contain data at each scan position. These regions where data does not exist are shown as white. This fidelity loss is caused by the nature of the measurement technique [23] as previously described and illustrated in Fig. 1. The measurement sensitivity is an inherent disadvantage of the ICI system. However, the region of lost signal distinctly shows the vapor depression shifted behind the process beam when comparing the 50 mm/s travel speed (Fig. 7b) to the 25 mm/s travel speed

(Fig. 7a). The process beam center is located at the x-y (0,0) position, and the beam diameter at the focal position is denoted by the circle.

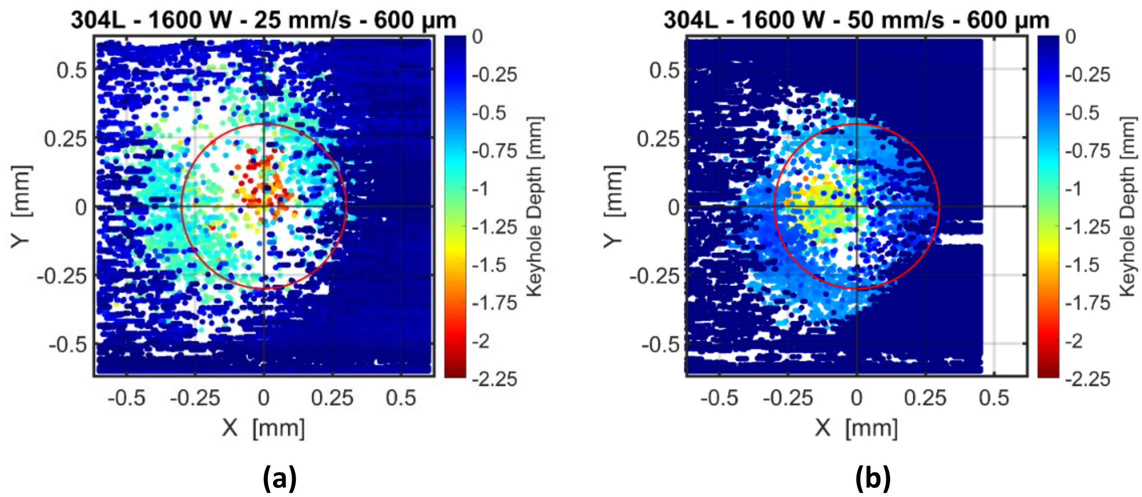

Figure 7. ICI keyhole tracking scans on 304L SS at 1600 W. Travel speeds at a) 25 mm/s and b) 50 mm/s. The crosshairs represent the process beam center. The circle represents the process beam diameter. The white represents no signal.

<u>Keyhole Position</u>

A distinct representation of the keyhole shift for 304L SS at 1600 W is shown in Figure 8. The images are a projection of the longitudinal (x-z) orientation with the travel direction from left to right. The beam diameter is represented by the dashed lines. It should be noted that this excludes the beam divergence after the focal position, but the divergence was negligible based on the measured 40 μm diameter difference at 2.94 mm below the focal point (i.e., plate surface) [29].

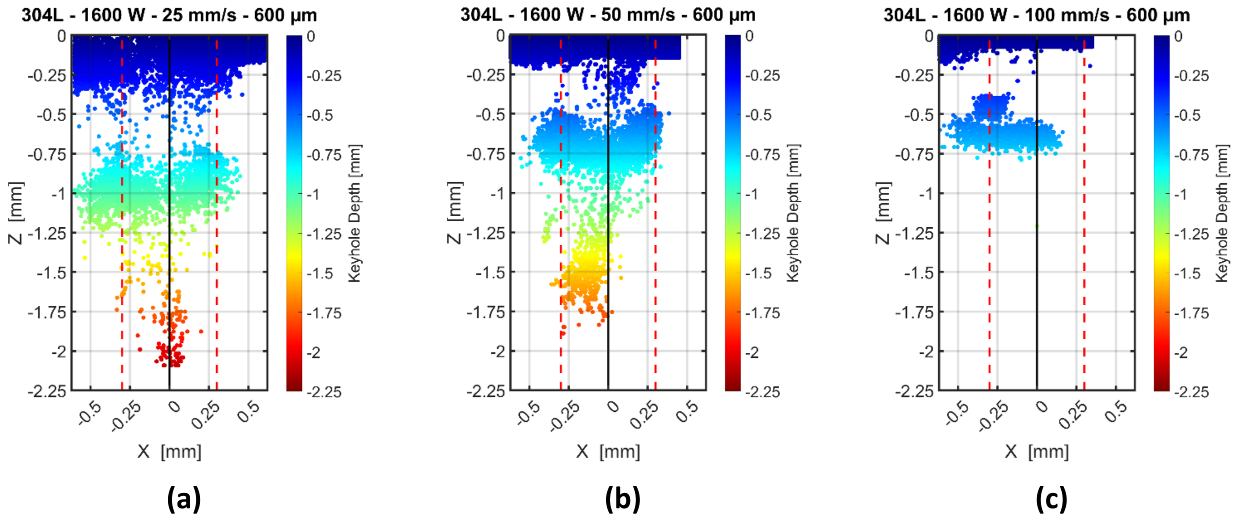

Figure 8. ICI keyhole tracking scans on 304L SS at 1600 W. Travel speeds at a) 25 mm/s, b) 50 mm/s, and c) 100 mm/s. The weld travel direction is left to right. The solid, black line represents the process beam center. The dotted, red line represents the beam diameter.

As the travel speed increased from 25 mm/s (Fig. 8a) to 50 mm/s (Fig. 8b), there was a reduction in the detected keyhole depth and a shift in the keyhole location. The 50 mm/s travel speed moved the keyhole root towards the back edge of the process beam. Further increasing the travel speed to 100 mm/s removed the high aspect ratio or keyhole portion of the vapor cavity, but a weld pool depression remained detectable as shown in Fig. 8c. This depression further lagged the process beam as compared to the slower travel speeds. Similar weld pool depression results were reported by Cunningham et al. [21] during *in-situ* x-ray imaging. It is unknown if the point cloud near 0.75 mm of depth at the 100 mm/s travel speed is truly a physical phenomenon and not an artifact of the detection technique. Error in the measurements may be due to vibrations in the optics caused by high acceleration, focal position discrepancies, and/or false reflection indications (Fig. 1).

Comparison of the 2205 DSS and Ti-6Al-4V keyhole results at the same parameters as 304L SS are shown in Fig. 9 and Fig. 10, respectively. Scans performed on Ti-6Al-4V showed a distinct difference in the acquired ICI data, while the increased keyhole depths contained fewer depth measurements, particularly near the keyhole root. Similar fidelity loss issues for nonferrous alloys as compared to steels were also reported by Dorsch et al. [30]. It is speculated that the reduced signal may be a result of plume formation and attenuation of the ICI beam.

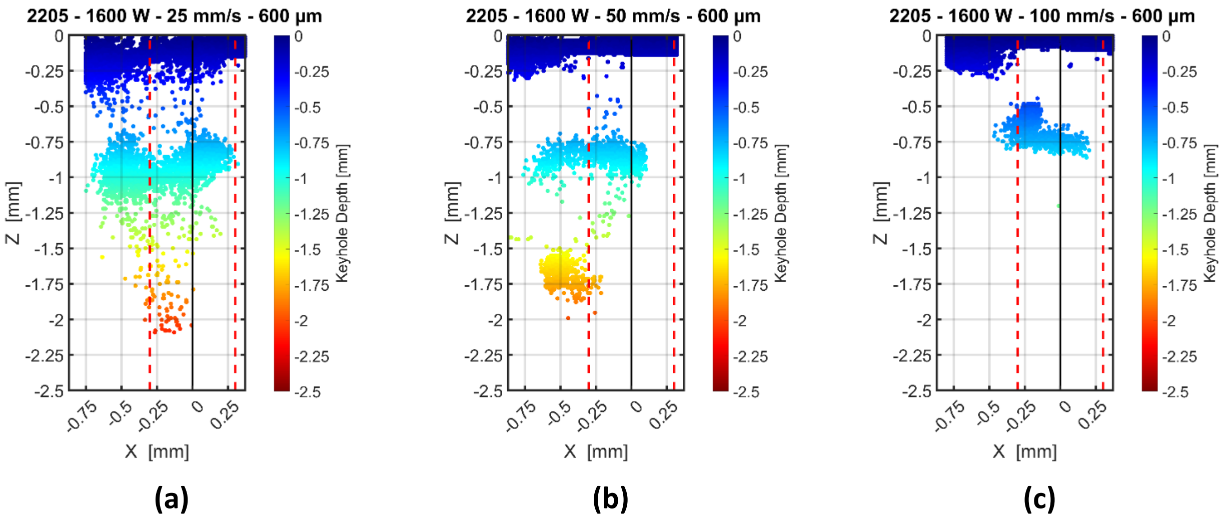

Figure 9. ICI keyhole tracking scans on 2205 DSS at 1600 W. Travel speeds at a) 25 mm/s, b) 50 mm/s, and c) 100 mm/s. The weld travel direction is left to right. The solid, black line represents the process beam center. The dotted, red line represents the beam diameter.

For comparison, the compilation of keyhole measurement data at 1000 W is provided in Figures 17-19 in the Appendix. During high aspect ratio welding, the 2205 DSS maintained the greatest keyhole shift behind the process beam followed by 304L SS. By measuring the deepest location of the keyhole relative to the process beam center, the lag of the keyhole was determined for each alloy and weld condition. Figure 11 shows plots at 1000 W and 1600 W of power in relation to travel speed for 304L SS, 2205 DSS, and Ti-6Al-4V.

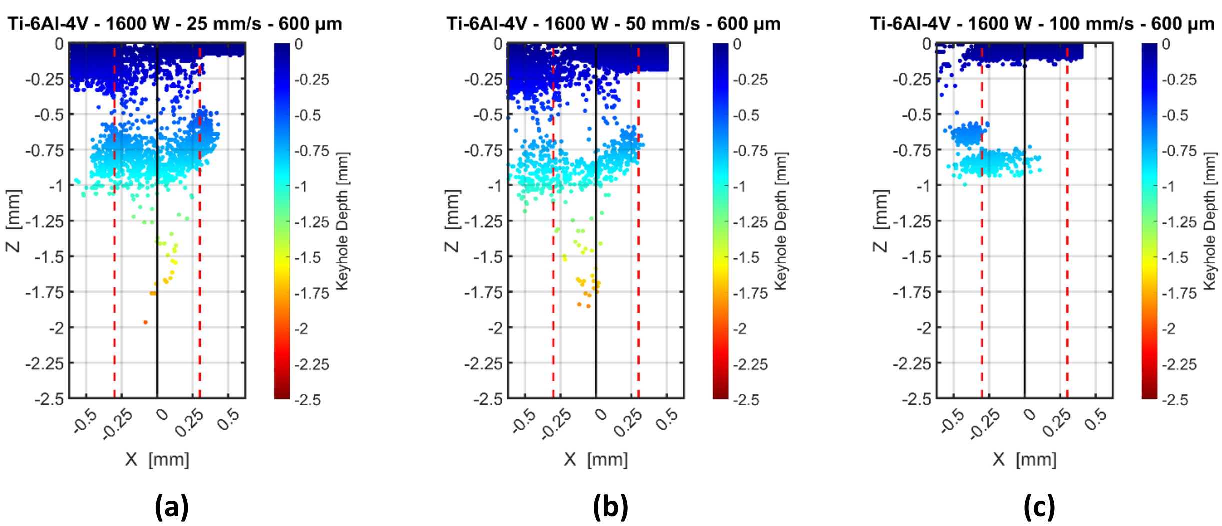

Figure 10. ICI keyhole tracking scans on Ti-6Al-4V at 1600 W. Travel speeds at a) 25 mm/s, b) 50 mm/s, and c) 100 mm/s. The weld travel direction is left to right. The solid, black line represents the process beam center. The dotted, red line represents the beam diameter.

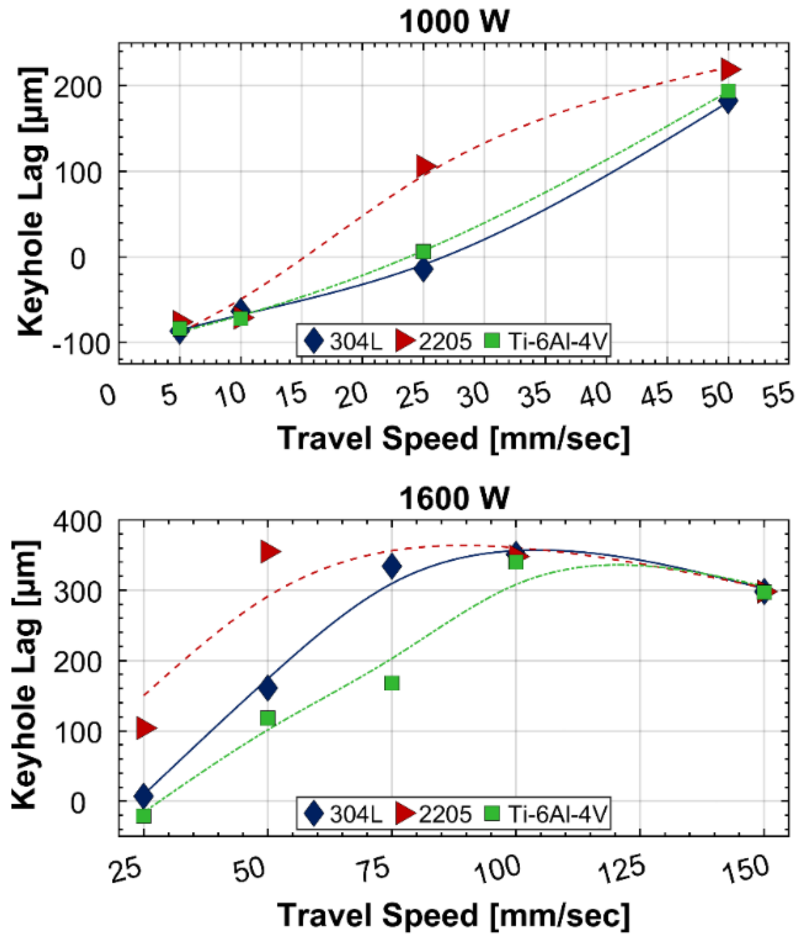

(a)

(b)

Figure 11. Keyhole lag for 304L SS, 2205 DSS, and Ti-6Al-4V at constant power and beam diameter of 600 µm. a) 1000 W, b) 1600 W. The best fit lines are solely for visualization purposes. The solid, blue line is for 304L SS. The dashed, red line is for 2205 DSS, and the dotted, green line is for Ti-6Al-4V.

At 1000 W (3.5 kW/mm^2) and relatively slow travel speeds, the keyhole root shifted towards the leading edge of the process beam (Fig. 11a) and was consistent for all alloys. Transitioning from the high aspect ratio welds near 25 mm/s showed higher keyhole lag for 2205 DSS, but 304L SS and Ti-6Al-4V showed nearly the same keyhole root positions at 1000 W of power.

Increasing the power to 1600 W (5.7 kW/mm^2) maintained the greatest keyhole lag with 2205 followed by 304L SS and Ti-6Al-4V, respectively (Fig. 11b). This material dependent lag only occurs during deep penetration, high aspect ratio welding. Once the power density or interaction time is reduced enough to favor low aspect ratio welds, the vapor depression lags toward the back of the process beam regardless of the alloy. However, fully characterizing these low aspect ratio welds with a minimal amount of weld pool depression was skewed due to excessive noise in the data. This was particularly more evident at higher travel speeds.

A result of this study revealed that Ti-6Al-4V showed reduced keyhole lag, which correlated to deeper weld penetration as shown in Figures 5 and 6. ~~It is~~ hypothesized that the keyhole lag is mostly related to the overall vaporization potential of the alloy, which results in greater beam absorption efficiency and deeper weld penetration. Sufficiently quantifying the influence of vaporization between each alloy is difficult due to composition, temperature, pressure, and fluid flow dependencies. Most vaporization research is for conduction mode welds and has been analyzed via modeling, with validation based on the constituents detected in the plume [45,46]. A major limitation of model results is due to difficult to measure material properties, which compound the inability to accurately predict vaporization and beam-matter interactions.

The keyhole position results are crucial for better understanding the beam interaction with the workpiece. If the lag of the keyhole increases behind the process beam, the incident laser energy cannot propagate into the depths of the cavity and be fully absorbed into the workpiece. Thus, the energy may become projected onto material in front of the weld that is assumed to be solid and oriented normal to the incident beam. If this assumption is valid, there will be significant variation in the beam coupling efficiency in relation to the process parameters. Another influential factor is the absorption of beam energy along the keyhole wall. Altering the wall angle will change the absorption and the heat flow across the vapor–liquid–solid interface [16–18]. Also, the beam will become distributed across an angled surface that is no longer representative of the beam diameter of 600 μm normal to the beam axis.

Keyhole Geometry

For an additional understanding of the keyhole, a surface fitting algorithm was coded in MATLAB® to analyze the ICI compiled depth measurements. The script used in this study was a modified version as reported in Reference [29]. Absent regions of data from the measurement matrix and the noise in the data necessitated the combination of fitting operations such as identifying outliers and incorporating moving mean smoothing operations. Specifically, the algorithm extracts vectors of data in one dimension (rows) and fits a linear equation between each data point to create a new matrix. The algorithm then extracts the vectors in the opposite dimension (columns) and repeats the same procedure. This was necessary for effectively processing the original data matrix with missing data points. Using this linearly fit data, a new data matrix is created based on the average of both matrices. An iteration is then performed on the averaged matrix to find peak values of each vector in the x (row) and y (column) dimensions. The peak values were then refit with linear interpolation and smoothed using a moving mean. This was performed in both dimensions, and the matrices were averaged together. These are the meshed data matrices further analyzed and presented. Figures 8-10 are projections of all the data solely for visualization and do not represent a cross-section or vector of data near the keyhole center.

The surface fitting results for 304L SS, 2205 DSS, and Ti-6Al-4V at 1000 W and 1600 W are shown in Figures 12 and 13, respectively. It should be noted that the wall angle between the detected transition and the pool surface may contain a different appearance than that produced by the fitting algorithm. If the vapor cavity were to bulge outward in a spherical or elliptical shape or taper behind the beam and underneath the weld pool, the geometry would not be detectable via the ICI system.

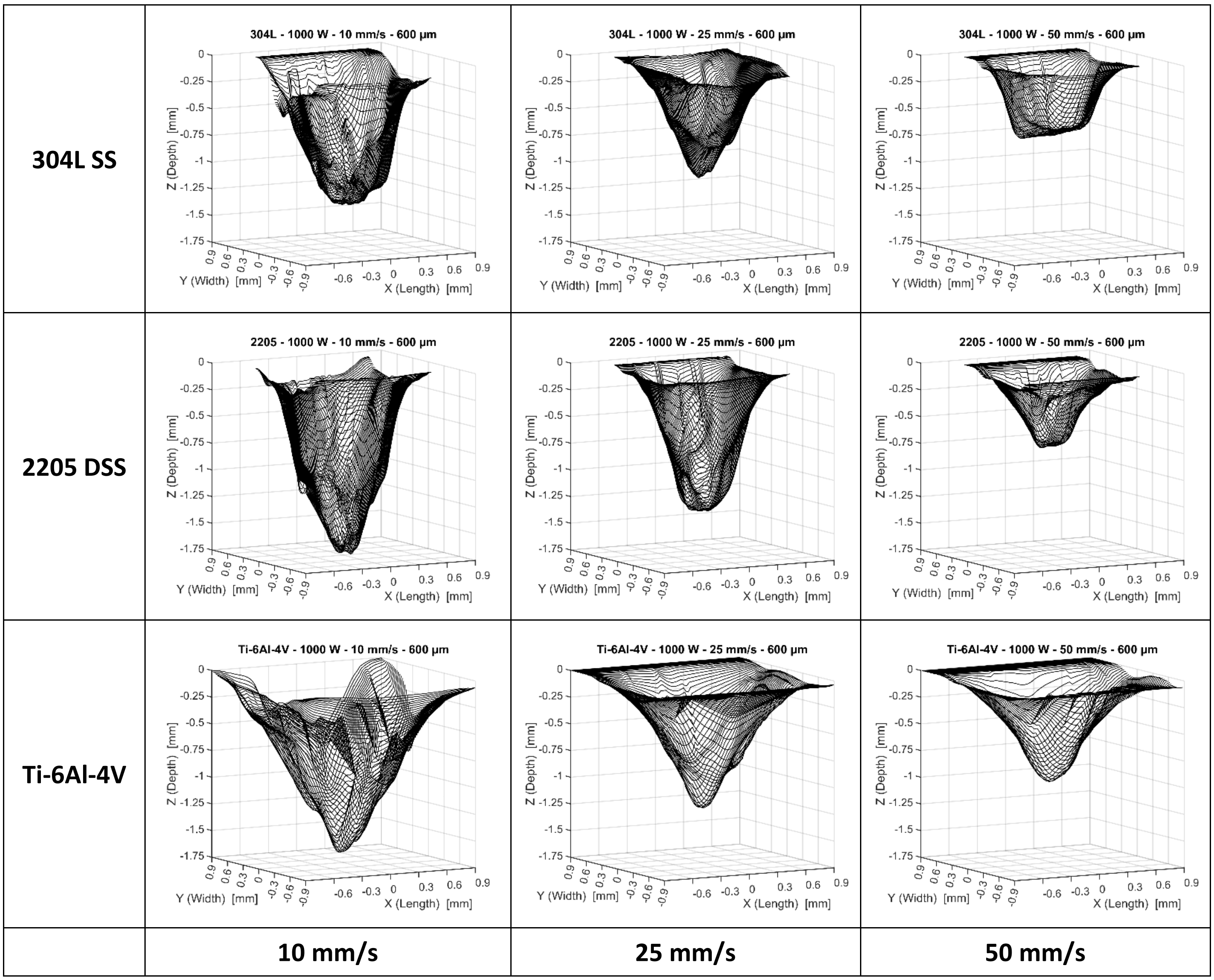

Figure 12. Surface fit ICI data at 1000 W for 304L SS, 2205 DSS, and Ti-6Al-4V. Travel was in the positive x-direction.

Analysis of the keyhole geometry indicated that a weld pool depression is present during low aspect ratio welds characterized as conduction mode. At the magnitudes detected, a weld pool depression indicates the significance of vaporization during all HED welding regimes. The transition to high aspect ratio welds progressed via a protrusion, commonly referred to as a "finger", out of the conduction-like weld shape. Conformation of vapor cavities with a reduced radius protruding from the conduction-like pool shape is supported by the transverse macrographs (Fig. 5 and 6). The protrusion out of the conduction-shaped weld pool is particularly evident in the macrographs of 304L SS and 2205 DSS at 1000 W and 50 mm/s. Prior work has shown that vaporization along the root alters the weld pool shape from a conventional arc-based conduction mode weld [29]. Because the vaporized root alters the weld pool shape and solidification conditions, a distinct region shows up in the etched response of the 304L SS and the 2205 DSS weld metal. These distinctions are fundamentally attributed to variations in dendrite or cell spacing and elemental partitioning.

Based on these keyhole results, it is argued that conduction mode, or low aspect ratio, welds may maintain a considerable amount of vaporization, which imparts a back pressure to sufficiently depress the weld pool surface. At some interaction time or power density, the recoil forces from vaporization can sufficiently overcome the surface tension along the root of the depression and penetrate deeper into the workpiece.

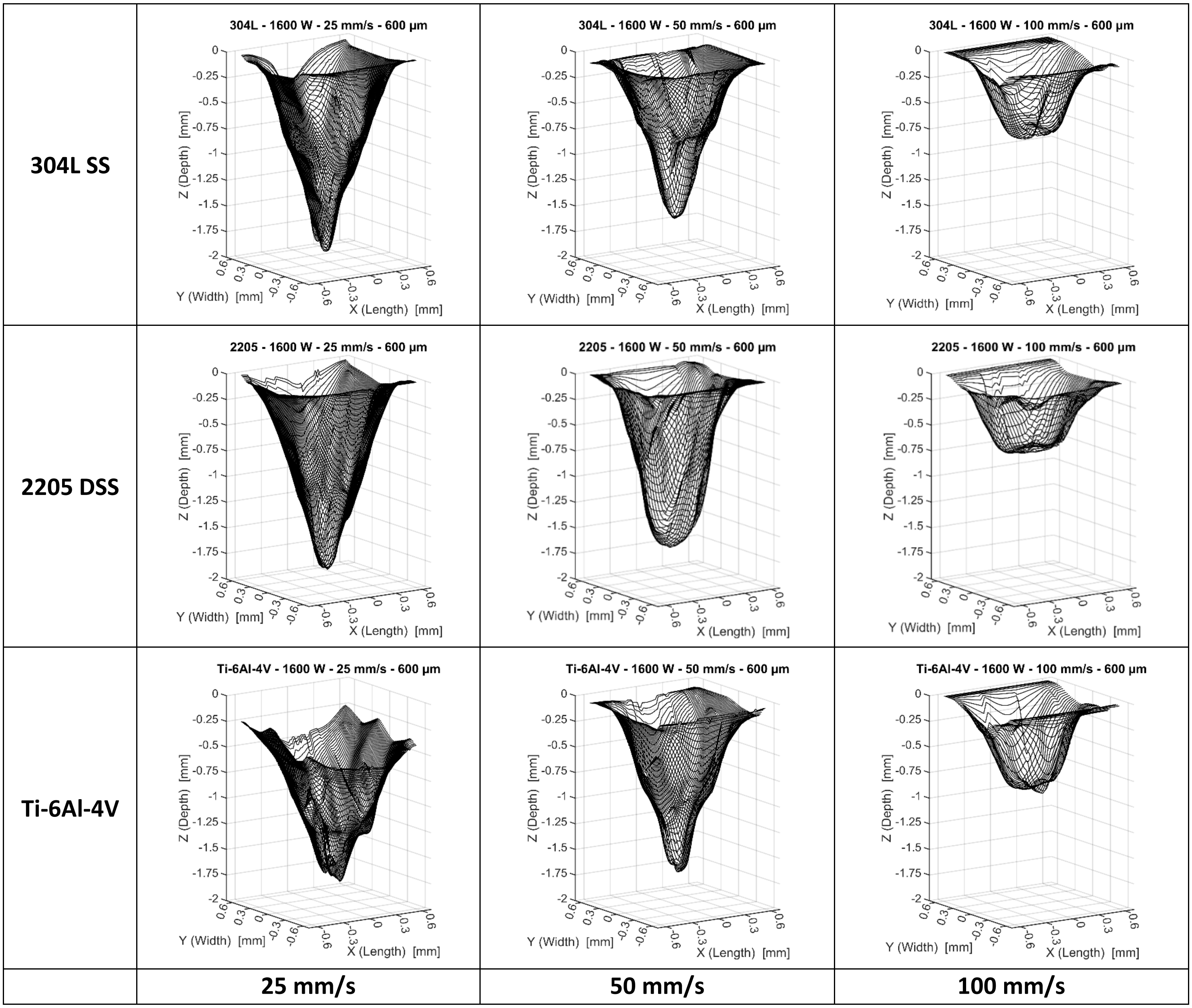

Figure 13. Surface fit ICI data at 1600 W for 304L SS, 2205 DSS, and Ti-6Al-4V. Travel was in the positive x-direction.

Using the surface fitting results, the keyhole volumes and diameters were estimated for each weld condition. The diameter results presented were taken using a full-width-half-maximum (FWHM) approach, which is based on the diameter at half the keyhole depth. The keyhole volumes at 1000 W and 1600 W are plotted in Figures 14a and 14b, respectively. The keyhole diameters at the same powers are plotted in Figures 15a and 15b, respectively.

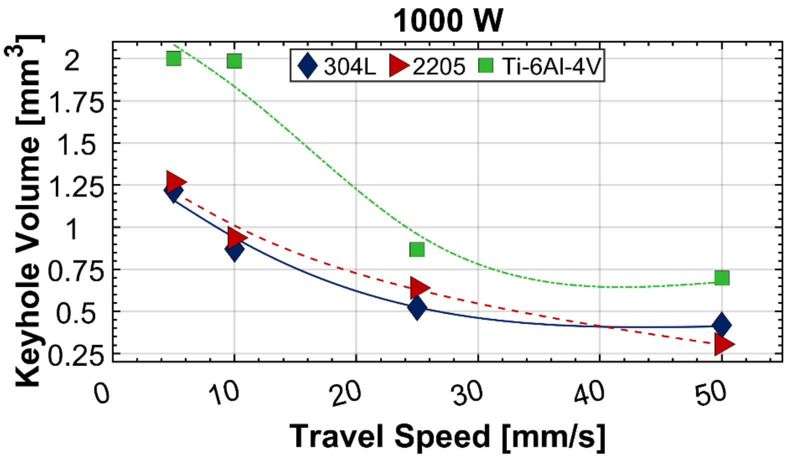

(a)

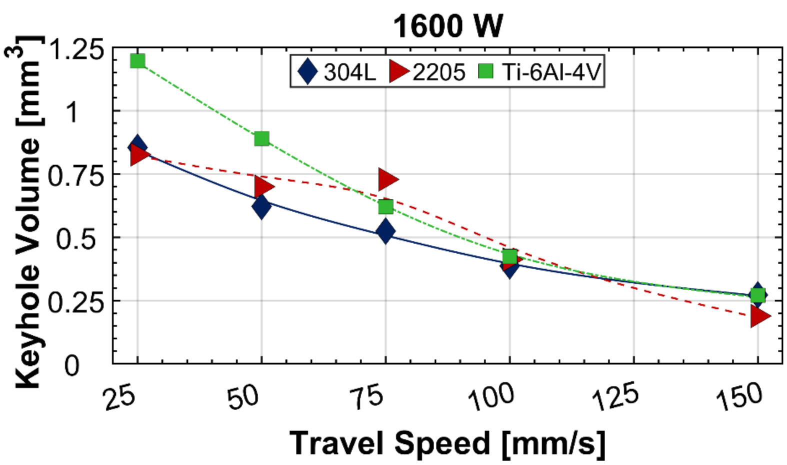

(b)

Figure 14. Change in keyhole volume for 304L SS, 2205 DSS, and Ti-6Al-4V. a) 1000 W, b) 1600 W. The best fit lines are solely for visualization purposes. The solid, blue line is for 304L SS. The dashed, red line is for 2205 DSS, and the dotted, green line is for Ti-6Al-4V.

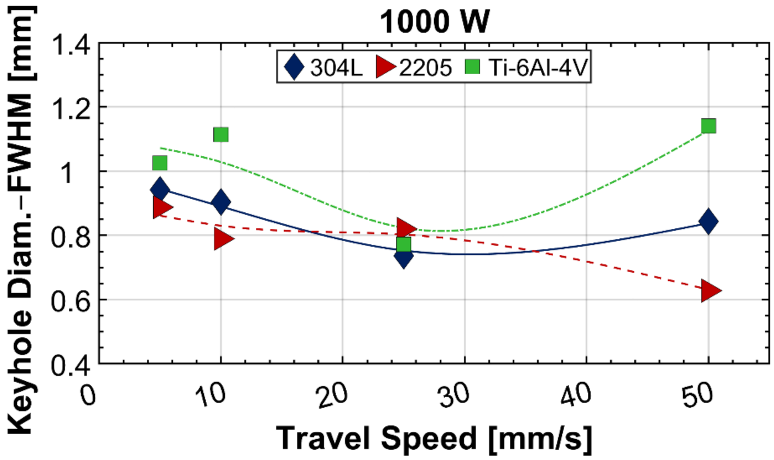

(a)

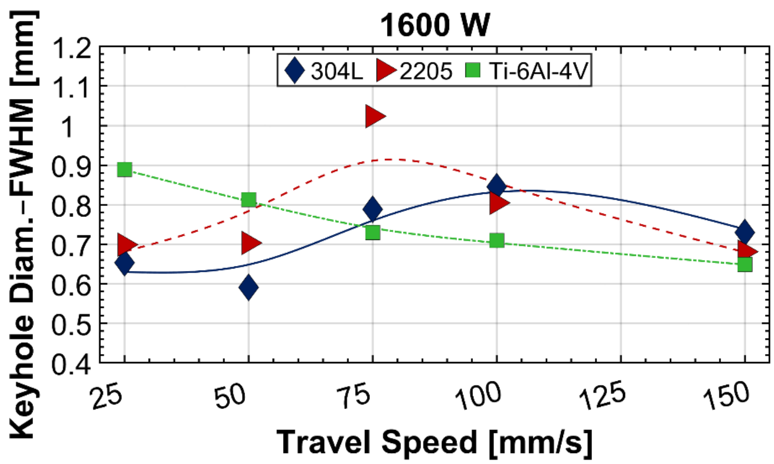

(b)

Figure 15. Change in keyhole diameter for 304L SS, 2205 DSS, and Ti-6Al-4V. a) 1000 W, b) 1600 W. The best fit lines are solely for visualization purposes. The solid, blue line is for 304L SS. The dashed, red line is for 2205 DSS, and the dotted, green line is for Ti-6Al-4V.

Approximating the keyhole volume was performed through a summation of the grid/mesh size of the surface fit and each depth value. Ti-6Al-4V showed the largest keyhole volume for nearly every parameter, which corresponded to a greater weld penetration, keyhole depth, and reduced keyhole lag. Thus, the material properties for Ti-6Al-4V (i.e., energy loss and vaporization potential) result in greater vaporization and melting as compared to 304L SS and 2205 DSS. The 304L SS and 2205 DSS maintained similar keyhole volumes, contrary to the keyhole lag results. Although the FWHM diameter measurement resulted in significant scatter and undefinable relationships, the behavior is similar and correlates to measuring the transverse section weld width as analyzed in Reference [29]. However, all the measured diameters were at or greater that the beam diameter. The measurements in the high aspect ratio welds showed keyhole diameters nearly 1.5X the beam diameter.

Historically, depth-to-width aspect ratios greater than 1-1.5 [1,2] are used to distinguish the transition from conduction to keyhole mode welding. This is under the assumption that weld toe was/is used as the location for determining the weld width. However, the indication of keyhole formation related to a weld toe-based aspect ratio is not a reliable distinction between conduction and keyhole mode, assuming keyhole refers to the creation of a vapor capillary within the liquid pool. ICI results along with macrophotos are shown in Fig. 16 to illustrate the comparison between a detected vapor cavity and low aspect ratio weld.

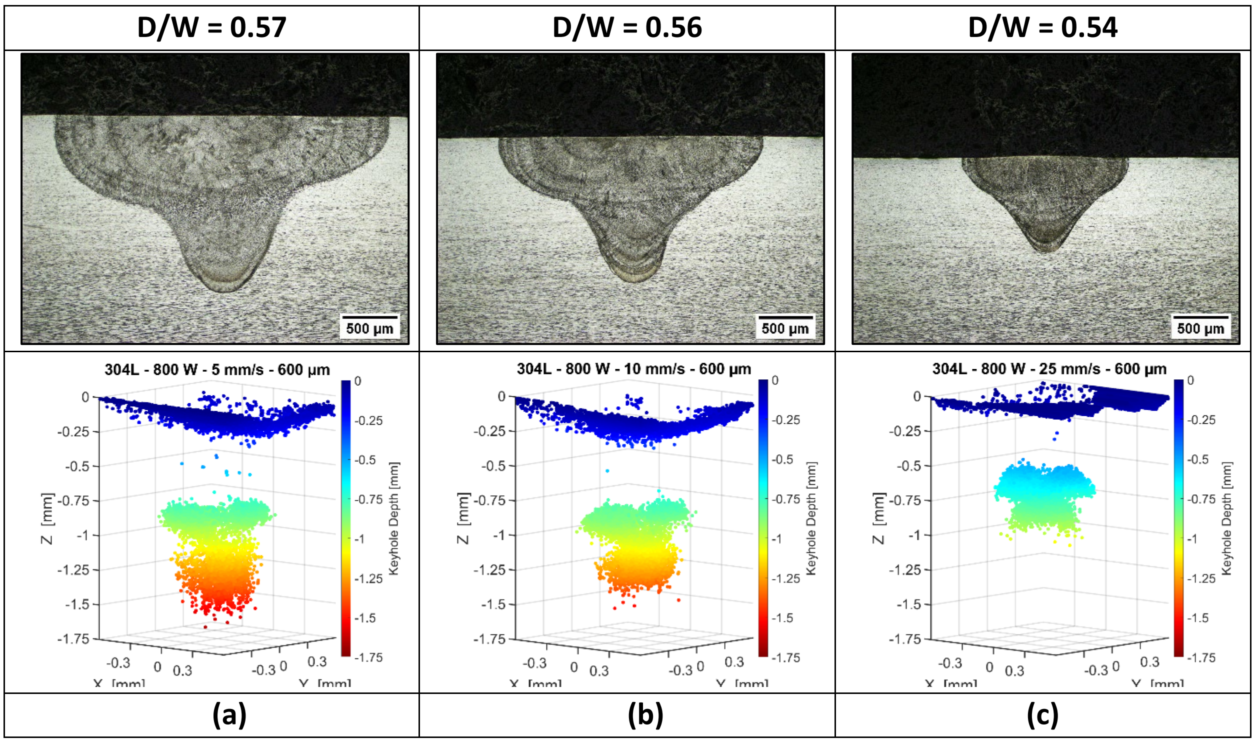

Figure 16. Welds made on 304L SS at 800 W containing low aspect ratios but maintaining keyholes as confirmed through ICI analysis. a) 5 mm/s, b) 10 mm/s, and c) 25 mm/s.

There is a clear indication of a keyhole from the ICI results at 800 W and travel speeds of 5 mm/s (Fig. 16a) and 25 mm/s (Fig. 16b). Analysis of the weld macrophotos showed measured depth-to-width aspect ratios around 0.5 when using toe width and lower than the generalized value near 1-1.5. If the depth-to-width analysis is performed using the FWHM weld width or centroid weld width, the 800 W and 25 mm/s weld has an aspect ratio near 1.0, and therefore, indicates the cusp for keyhole formation, which is confirmed based on the macrophoto and ICI data.

Summary and Outlook

The ICI system was able to map the vapor depression within the weld pool but showed significantly lower resolution at higher depths, especially with Ti-6Al-4V. These results demonstrated how the keyhole or weld pool depression shifted further behind the process beam with increasing travel speed. The keyhole lag was shown to be material dependent, with the lag greatest in 2205 DSS and least with Ti-6Al-4V. The transition of the keyhole behind the process beam showed a correlation with reduced weld penetration and keyhole volume. Trends were not detected between the process parameters and the keyhole diameter measurements, but the results are consistent with weld width measurements from the transverse metallographic sections.

Although there is a clear differentiation between deep penetration and shallow welds, there was no definitive transition that defined the shift from “conduction” to “keyhole” mode. As reported in this study, there was always a detectable vapor cavity or depression, regardless of the weld cross-section appearing as “conduction” mode or having a low aspect ratio (depth-to-width) less than one.

An important outcome of this work demonstrates the need for numerical models to accurately incorporate both surface tension and vaporization from conduction to keyhole mode welds. Keyholes are not simply cylindrical or slender vapor cavities that penetrate the workpiece at approximately the same diameter as the process beam [16,17,19]. Rather, there is a complex interaction that incorporates beam diameter, power density, incident angle, and material properties [1,4,11,47].

Conclusions

The main conclusions for this study are summarized as follows:

1) The ICI system detected a weld pool depression at all parameters and alloys investigated, indicating the presence of vaporization and a resulting back pressure that creates a vapor cavity.
2) The vapor capillary lagged the process beam at higher travel speeds and/or lower powers. The 2205 DSS showed the greatest keyhole lag followed by 304L SS and Ti-6Al-4V.
3) Overall, Ti-6Al-4V maintained the largest keyhole volume across all parameters. Minimal differences in the keyhole volume were apparent between 304L SS and 2205 DSS. The volume results correlated with reduced keyhole lag and greatest keyhole depth.
4) Full width half maximum (FWHM) beam diameter measurements ranged from the beam diameter (600 µm) to nearly 1.5X the beam diameter. However, a distinguishable trend was not evident.

5) Distinguishing conduction versus keyhole mode welding based on a depth-to-width aspect ratio of 1-1.5 is insufficient unless transverse section weld width measurements are clearly defined as FWHM or centroid widths.

Acknowledgements

This research was made possible via the National Science Foundation (NSF) sponsored Industry/University Cooperative Research Center (I/UCRC): Manufacturing and Materials Joining Innovation Center (Ma2JIC) based on grant number 1822144.

The authors would like to recognize Los Alamos National Laboratory (LANL) for their financial support and, in particular, Dr. Matt Johnson and Dr. David Tung who served as the project mentors. In addition, the authors would like to acknowledge IPG Photonics®, specifically, Kevin Arnold and the Midwest Operations group for supporting the development of the Ohio State University's high-power laser welding laboratory.

References

[1] American Welding Society. Laser Beam Welding, Cutting, and Associated Processes. In: Kautz D, Merchant VE, Milewski JO, Powers DE, editors. Weld. Handb. Vol. 3 Weld. Process. Part 2. 9th ed., Miami, Florida, USA: American Welding Society; 2007, p. 503–60.

[2] Amada Miyachi America I. Laser Welding Fundamentals 2016.

[3] Russo AJ, Akau RL, Jellison JL. Thermocapillary Flow in Pulsed Laser Beam Weld Pools. Weld J 1990;69:23–9.

[4] Webber T, Lieb T, Mazumder J. Laser Beam Welding. In: Lienert T, Siewert T, Babu S, Acoff V, editors. ASM Handbook, Vol. 6A, Weld. Fundam. Process., vol. 6A, ASM International; 2011, p. 556–69. https://doi.org/10.31399/asm.hb.v06a.a0005641.

[5] Cho JH, Farson DF, Reiter MJ. Analysis of Penetration Depth Fluctuations in Single-mode Fibre Laser Welds. J Phys D Appl Phys 2009;42. https://doi.org/10.1088/0022-3727/42/11/115501.

[6] Lee JY, Ko SH, Farson DF, Yoo CD. Mechanism of Keyhole Formation and Stability in Stationary Laser Welding. J Phys D Appl Phys 2002;35:1570–6. https://doi.org/10.1088/0022-3727/35/13/320.

[7] Matsunawa A. Science of Laser Welding - Mechanisms of Keyhole and Pool Dynamics. ICALEO 2002 - 21st Int. Congr. Appl. Laser Electro-Optics, Congr. Proc., vol. 290, Laser Institute of America; 2002. https://doi.org/10.2351/1.5065734.

[8] Matsunawa A, Kim J, Katayama S, Seto N, Mizutani M, Katayama S. Dynamics of Keyhole and Molten Pool in Laser Welding. J Laser Appl 1998;10:247–54. https://doi.org/10.2351/1.521858.

[9] Robertson SM, Kaplan AFH, Frostevarg J. Material ejection attempts during laser keyhole

welding. J Manuf Process 2021;67:91–100. https://doi.org/10.1016/j.jmapro.2021.04.052.

[10] Elmer JW, Hochanadel PW, Lachenberg K, Webber T. Introduction to High Energy Density Electron and Laser Beam Welding. In: Lienert T, Siewert T, Babu S, Acoff V, editors. ASM Handbook, Vol. 6A, Weld. Fundam. Process., vol. 6A, ASM International; 2011, p. 507–13. https://doi.org/10.31399/asm.hb.v06a.a0005627.

[11] Assunção EG. Investigation of Conduction to Keyhole Mode Transition. Cranfield University, 2012.

[12] Eriksson I, Powell J, Kaplan AFH. Melt Behavior on the Keyhole Front during High Speed Laser Welding. Opt Lasers Eng 2013;51:735–40. https://doi.org/10.1016/j.optlaseng.2013.01.008.

[13] Katayama S, Seto N, Kim J Do, Matsunawa A. Formation Mechanism and Reduction Method of Porosity in Laser Welding of Stainless Steel. Laser Inst Am Proc 1997;83. https://doi.org/10.2351/1.5059741.

[14] Miyagi M, Wang J. Keyhole Dynamics and Morphology Visualized by in-situ X-ray Imaging in Laser Melting of Austenitic Stainless Steel. J Mater Process Technol 2020;282. https://doi.org/10.1016/j.jmatprotec.2020.116673.

[15] Dowden J, Davis M, Kapadia P. The Flow of Heat and the Motion of the Weld Pool in Penetration Welding with a Laser. J Appl Phys 1985;57:4474–9. https://doi.org/10.1063/1.334571.

[16] Kaplan AFH. A Model of Deep Penetration Laser Welding Based on Calculation of the Keyhole Profile. J Phys D Appl Phys 1994;27:1805–14. https://doi.org/10.1088/0022-3727/27/9/002.

[17] Rai R, Elmer JW, Palmer TA, Debroy T. Heat Transfer and Fluid Flow during Keyhole Mode Laser Welding of Tantalum, Ti-6Al-4V, 304L Stainless Steel and Vanadium. J Phys D Appl Phys 2007;40:5753–66. https://doi.org/10.1109/JQE.1974.1145810.

[18] Rai R, Burgardt P, Milewski JO, Lienert TJ, Debroy T. Heat Transfer and Fluid Flow during Electron Beam Welding of 21Cr-6Ni-9Mn Steel and Ti-6Al-4V Alloy. J Phys D Appl Phys 2009;42. https://doi.org/10.1088/0022-3727/42/2/025503.

[19] Jiang M, Chen YB, Chen X, Toa W, Debroy T. Enhanced Penetration Depth during Reduced Pressure Keyhole-Mode Laser Welding. Weld J 2020;99:110–24. https://doi.org/10.29391/2020.99.011.

[20] Boley M, Abt F, Weber R, Graf T. X-ray and Optical Videography for 3D Measurement of Capillary and Melt Pool Geometry in Laser Welding. Phys Procedia 2013;41:488–95. https://doi.org/10.1016/j.phpro.2013.03.105.

[21] Cunningham R, Zhao C, Parab N, Kantzos C, Pauza J, Fezzaa K, et al. Keyhole threshold and morphology in laser melting revealed by ultrahigh-speed x-ray imaging. Science (80-) 2019;363:849–52.

[22] Arata V. Fundamental Characteristics of High Energy Density Beams in Material Processing. Int. Congr. Appl. Lasers Electro-Optics, vol. 73, Laser Institute of America; 1986, p. 73–9. https://doi.org/10.2351/1.5057871.

[23] Boley M, Webster P, Heider A, Weber R, Graf T. Investigating the Keyhole Behavior by using X-ray and Optical Depth Measurement Techniques 2014:426–30.

https://doi.org/10.2351/1.5063091.
[24] Ji Y, Grindal AW, Webster PJLL, Fraser JM. Real-time Depth Monitoring and Control of Laser Machining through Scanning Beam Delivery System. J Phys D Appl Phys 2015;48. https://doi.org/10.1088/0022-3727/48/15/155301.
[25] Webster PJLL, Wright LG, Mortimer KD, Leung BY, Yu JXZZ, Fraser JM. Automatic Real-time Guidance of Laser Machining with Inline Coherent Imaging. 29th Int. Congr. Appl. Lasers Electro-Optics, ICALEO 2010 - Congr. Proc., vol. 103, Laser Institute of America; 2010, p. 1386–93. https://doi.org/10.2351/1.3567955.
[26] Webster PJL, Yu JXZ, Leung BYC, Wright LG, Mortimer KD, Fraser JM. Inline Coherent Imaging of Laser Micromachining. 2010 Int. Symp. Optomechatronic Technol., IEEE; 2010. https://doi.org/10.1109/ISOT.2010.5687305.
[27] Fraser JM. Laser Process Monitoring and Automatic Control at kHz Rates through Inline Coherent Imaging. AIP Conf Proc 2012;1464:492–6. https://doi.org/10.1063/1.4739903.
[28] Patterson T, Hochanadel J, Sutton S, Panton B, Lippold J. A Review of High Energy Density Beam Processes for Welding and Additive Manufacturing Applications. Weld World 2021;65:1235–306. https://doi.org/10.1007/s40194-021-01116-0.
[29] Patterson T. Understanding Weld Formation and Microstructure Evolution in Laser Welded Stainless Steels and Ti-6Al-4V. The Ohio State University, 2021.
[30] Dorsch F, Dubitzky W, Hermani J-P, Hromadka A, Hesse T, Notheis T, et al. Controlling Laser Processing via Optical Coherence Topography. In: Kaierle S, Heinemann SW, editors. High-Power Laser Mater. Process. Appl. Diagnostics, Syst. VIII, SPIE; 2019. https://doi.org/10.1117/12.2509630.
[31] Fleming TG, Nestor SGL, Allen TR, Boukhaled MA, Smith NJ, Fraser JM. Tracking and Controlling the Morphology Evolution of 3D Powder-bed Fusion in situ using Inline Coherent Imaging. Addit Manuf 2020;32. https://doi.org/10.1016/j.addma.2019.100978.
[32] Fraser JM. Inline Coherent Imaging of Laser Processing. Front Ultrafast Opt Biomed Sci Ind Appl XI 2011;7925:792516. https://doi.org/10.1117/12.877745.
[33] Webster PJL, Fraser JM, Yang VXD. Methods and Systems for Coherent Imaging and Feedback Control for Modification of Materials. US 8,822,875 B2, 2014. https://doi.org/10.1007/10877768.
[34] Webster PJL, Wright LG, Ji Y, Galbraith CM, Kinross AW, Van Vlack C, et al. Automatic Laser Welding and Milling with in situ Inline Coherent Imaging. Opt Lett 2014;39:6217–20. https://doi.org/10.1364/ol.39.006217.
[35] Boley M, Fetzer F, Weber R, Graf T. Statistical Evaluation Method to Determine the Laser Welding Depth by Optical Coherence Tomography. Opt Lasers Eng 2019;119:56–64. https://doi.org/10.1016/j.optlaseng.2019.03.014.
[36] PRIMES GmbH. FocusMonitor FM+ n.d.:1–7. https://www.primes.de/en/products/beam-distribution/focus-measurement/focusmonitor-fmplus.html (accessed November 2, 2021).
[37] International Standards Organization. ISO 11146-1:2005 Lasers and laser-related equipment – Test methods for laser beam widths, divergence angles and beam propagation ratios – Part1: Stigmatic and simple astigmatic beams 2005.
[38] IPG Photonics. Inline Coherent Imaging System Software Manual 2018.

[39] ASTM E1019-11: Standard Test Methods for Determination of Carbon, Sulfur, Nitrogen, and Oxygen in Steel and in Steel, Iron, Nickel, and Cobalt Alloys by Various Combustion and Fusion Techniques. West Conshohocken, PA, United States: ASTM International; 2011. https://doi.org/10.1520/E1019-18.2.

[40] ASTM E1941-10: Standard Test Method for Determination of Carbon in Refractory and Reactive Metals and Their Alloys by Combustion Analysis. West Conshohocken, PA, United States: ASTM International; 2016. https://doi.org/10.1520/E1941-10R16.2.

[41] ASTM E1409-13: Standard Test Method for Determination of Oxygen and Nitrogen in Titanium and Titanium Alloys by Inert Gas Fusion. West Conshohocken, PA, United States: ASTM International; 2013. https://doi.org/10.1520/E1409-13.2.

[42] ASTM E1447-09: Standard Test Method for Determination of Hydrogen in Titanium and Titanium Alloys by Inert Gas Fusion Thermal Conductivity / Infrared Detection. West Conshohocken, PA, United States: ASTM International; 2016. https://doi.org/10.1520/E1447-09R16.2.

[43] Patterson T, Lippold J, Panton B. Laser weld formation and microstructure evolution in stainless steel alloys. Weld World 2022. https://doi.org/10.1007/s40194-022-01285-6.

[44] Seidgazov RD. Thermocapillary Mechanism of Melt Displacement during Keyhole Formation by the Laser Beam. J Phys D Appl Phys 2009;42. https://doi.org/10.1088/0022-3727/42/17/175501.

[45] He X, Fuerschbach PW, Debroy T, Suder W, Williams S, Shinichi T, et al. Understanding Metal Vaporization from Laser Welding. J Phys D Appl Phys 2010;39:1–2. https://doi.org/10.1016/j.ijheatmasstransfer.2018.05.031.

[46] Fuerschbach PW, Norris JT, He X, Debroy T. Understanding Metal Vaporization from Laser Welding. 2003.

[47] Khan MS, Ali S, Westerbaan D, Duley W, Biro E, Zhou YN. The effect of laser impingement angle on the optimization of melt pool geometry to improve process stability during high-speed laser welding of thin-gauge automotive steels. J Manuf Process 2022;78:242–53. https://doi.org/10.1016/j.jmapro.2022.04.022.

Appendix

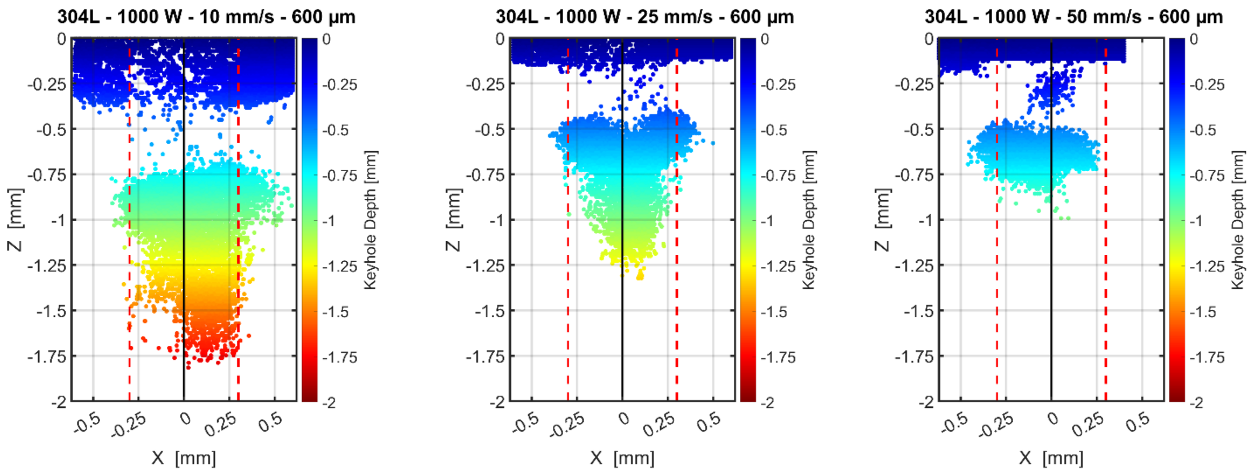

(a) (b) (c)

Figure 17. ICI keyhole tracking scans on 304L SS at 1000 W. Travel speeds at a) 10 mm/s, b) 25 mm/s, and c) 50 mm/s. The weld travel direction is left to right. The solid, black line represents the process beam center. The dotted, red line represents the beam diameter.

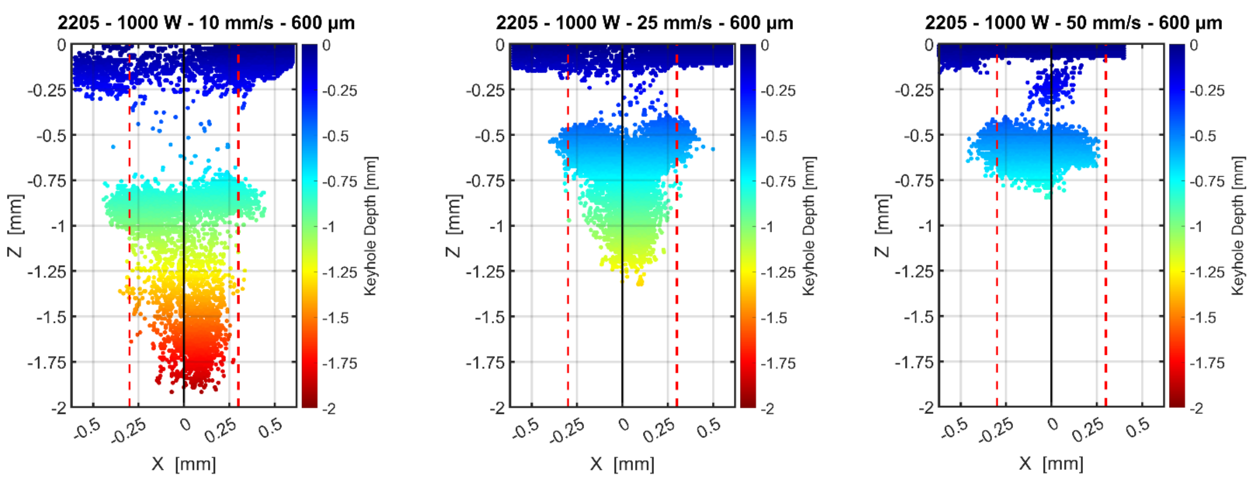

(a) (b) (c)

Figure 18. ICI keyhole tracking scans on 2205 DSS at 1000 W. Travel speeds at a) 10 mm/s, b) 25 mm/s, and c) 50 mm/s. The weld travel direction is left to right. The solid, black line represents the process beam center. The dotted, red line represents the beam diameter.

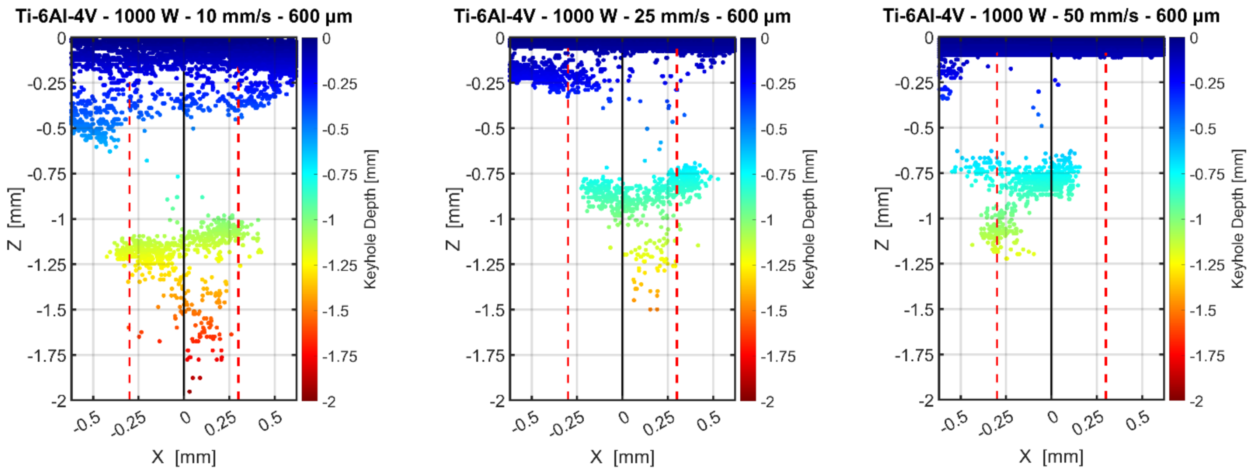

(a) **(b)** **(c)**

Figure 19. ICI keyhole tracking scans on Ti-6Al-4V at 1000 W. Travel speeds at a) 10 mm/s, b) 25 mm/s, and c) 50 mm/s. The weld travel direction is left to right. The solid, black line represents the process beam center. The dotted, red line represents the beam diameter.